Defence Technology 32 (2024) 405–411

Contents lists available at ScienceDirect

Defence Technology

journal homepage: www.keaipublishing.com/en/journals/defence-technology

Toughening ultrastrong low-density steel by textured δ-ferrite lamellas

Bin Hu [a, *, 1], Guosen Zhu [b, 1], Guohui Shen [a], Zheng Wang [a], Qinghua Wen [a], Xiao Shen [c], Haiwen Luo [a, **]

[a] School of Metallurgical and Ecological Engineering, University of Science and Technology Beijing, Xue Yuan Rd. 30, Beijing 100083, China
[b] Shougang Research Institute of Technology, Yangzhuang Street 69, Beijing 100043, China
[c] Steel Institute, RWTH Aachen University, Intzestraße 1, 52072, Aachen, Germany

ARTICLE INFO

Article history:
Received 21 March 2023
Received in revised form
23 April 2023
Accepted 8 May 2023
Available online 11 May 2023

Keywords:
Ultrastrong and light steel
δ-Ferrite lamellas
Crack propagation
Toughness

ABSTRACT

By both the Charpy V-notched impact and the projectile tests, we here investigated the dynamic fracture behavior of a recently developed ultrastrong lightweight steel comprising a hierarchical martensitic matrix, dispersed ultra-fine-retained austenite grains and oriented δ-ferrite lamellas, the latter being due to high Al and Si contents employed for low-density design. This steel shows a superior combination of specific ultimate tensile strength and impact toughness to other ultrastrong steels and has successfully arrested a real steel-cored bullet shot. These are attributed to the densely textured δ-ferrite lamellas that can deflect the propagating cracks until they are trapped and enclosed besides austenite-to-martensite transformation crack closure, leading to more energy consumed before failure. These results suggest a new pathway for toughening ultrastrong lightweight steels.

1. Introduction

Ultrastrong but light steels have been long desired in the automotive, aviation, and defense industries to enhance engineering reliability and reduce CO_2 emissions [1]. Unfortunately, both the popular strengthening solutions and lightweight designs often sacrifice toughness [2,3], the latter measures the capability of materials of resisting the cracking either dynamically or statically and is strictly required in the safety design. A classical high-end application example of ultrastrong steel is the armored vehicle because it requires both improved maneuverability and travelling speed via reduced density and excellent ballistic performance [4]. The bulletproof properties could be improved by increasing both hardness/strength to suppress the plugging failure and toughness to avoid the brittle fracture during the ballistic test [5,6].

A general method of toughening ultrastrong steels is to increase the plastic energy consumed in the vicinity of the propagating crack that leads to the failure [7]. Therefore, a metal that can resist higher load and plastically deform more during deformation is more tough in general [8]. Recently, we have developed an ultrastrong tri-phase steel possessing an ultrahigh tensile strength (UTS) of 2112 MPa, total elongation (TE) of 16% at the reduced density of 7.39 g/cm^3 [9]. In addition to its ultrahigh tensile strength and good ductility, it also exhibits the extraordinary plastic-hardening capacity of 1360 MPa, which may also improve the bulletproof performance, because high-N austenitic stainless steel, having a relative low yield strength (YS) and high work hardening rate, behaves similarly to ultrastrong martensitic armor steels during the projectile tests [10]. Moreover, the microstructure of developed steel exhibited lamellated morphology [9], which is beneficial to improving the toughness at high strength and low density [11–14]. As an example, the laminated ferrite was introduced into the martensite matrix, leading to the Charpy V-notch toughness increasing by 10 times that of the conventional low alloy steels with the similar strength [14]. Therefore, such an excellent combination of tensile properties and lamellated microstructure may hint a possibly excellent toughness and then bulletproof performance too, making this ultrastrong steel ideally fit the application of armored vehicle. In this paper, both the standard Charpy V-notched (CVN) impact and ballistic tests were performed on this ultrastrong steel to examine

* Corresponding author.
** Corresponding author.
E-mail addresses: hubin@ustb.edu.cn (B. Hu), luohaiwen@ustb.edu.cn (H. Luo).
Peer review under responsibility of China Ordnance Society
[1] These authors contributed equally to this work.

https://doi.org/10.1016/j.dt.2023.05.006

its resistance to dynamic fracture; particularly, the cracking path in the tri-phase microstructure was traced carefully during the impact and projectile tests, leading to a new finding that a considerable amount of relatively soft and properly textured δ-ferrite lamellas could toughen rather than embrittle this ultrastrong steel by increasing the energy required to rupture it. Finally, we propose a new low-density microstructural design strategy for toughening ultrastrong steels and enhancing bulletproof capability.

2. Experimental methods

The studied steel plate was hot rolled and tempered, having a 4.9-mm thickness and the nominal composition of 0.38% C–6.74% Mn–1.27% Si–2.91% Al–0.38% V–0.034% Nb–0.0029% B (weight percentage unless mentioned elsewhere). It has a measured density of 7.36 ± 0.03 g/cm^3 by using the Archemedes principle and hardness of 62 HRC. The YS ($\sigma_{0.2}$), UTS, TE along the rolling and transverse directions (RD and TD) were measured as 1300 MPa, 2105 MPa, 16% and 1306 MPa, 2122 MPa, 13% respectively. Details on the compositional designing strategy and manufacturing process have been described elsewhere [9]. CVN impact tests were performed at −40 °C according to ASTM A370 on the V-notched specimens with the dimension of 55 mm (length) × 10 mm (width) × 4.9 mm (thickness). The CVN specimens were grooved on the ND (normal direction) × RD plane. The ballistic tests were conducted at zero obliquity, i.e. the projectile path was normal to the plane of the target plate. During the bulletproof tests, steel plate with the 407 mm × 135 mm size was clamped firmly to the target holder already positioned for an attack angle of 90°. The steel-cored projectiles with the diameter of 7.62 mm were fired with the muzzle velocity of 825–827 m/s from a gun at the distance of 80 m. According to the military standards on the ballistic tests, the center-to-center distance between any two impact craters on the plate must be at least four times as the diameter of the projectile, while the distance from the impact center to the edge of the plate must be at least twice as the projectile diameter. Wherever these distance criteria were not met, the craters were not considered for further analysis.

The microstructures were examined by field emission scanning electron microscope (FE-SEM), JSM-6710F, at 20 kV after polishing and etching in 4% nitric acid for 20 s. Electron backscattered diffraction (EBSD) examination was performed on an Auger Nano probe combined with EBSD (Nano-Auger/EBSD PHI 710) at 20 kV. The data were processed by EDAX OIM software. High-energy synchrotron X-ray diffraction (HEXRD) was employed to investigate the volume fraction of retained austenite (RA) around caters after ballistic test. The HEXRD experiments were conducted at the Powder Diffraction and Total Scattering Beamline P02.1 of PETRA III at Deutsches Elektronen Synchrotron (DESY) in Hamburg, Germany. The beamline was operated at a fixed energy of 60 keV, supplying a monochromatic X-ray with a wavelength of ~0.207 Å. RA fractions were calculated from the integrated intensities of (200)α, (211)α, (200)γ, (220)γ and (311)γ diffraction peaks, as detailed in Ref. [15]. Samples for EBSD and XRD examinations were electro-polished in a solution of 20% perchloric acid and 80% ethanol at room temperature.

3. Results

3.1. CVN impact tests

The V-notched impact toughness of studied steel along the transverse and longitudinal directions at −40 °C were measured as the 30 ± 2 J/cm^2 and 26.7 J/cm^2 respectively, which has been converted for being compared with the standard impact toughness values according to the proposed method in 'Ship Specifications' [16]. In Fig. 1, both CVN toughness and specific UTS of studied steel are compared with other steels having the UTS of 1.0–2.5 GPa [17–29]. It is seen that our developed steel has the superior combination of specific UTS and CVN toughness to any existing ultrastrong steel to date, to our knowledge.

SEM and EBSD results in Figs. 2(a) and 2(b) show that the initial microstructures have a martensitic (α′) matrix, where both ultrafine RA grains, and elongated δ-ferrite lamellas with a strong {200} in-plane texture parallel to the sheet surface (Fig. 2(c)) are dispersed. The δ-ferrite started to form during solidification due to the high Si and Al contents and was elongated to form a texture during hot rolling. The average diameters of prior austenite and RA grains were measured as 32 ± 6 μm and 0.73 ± 0.4 μm; while the length and thickness of δ-ferrite grains are 150–500 μm and 1–4 μm respectively. Figs. 2(d) and 2(e) are the morphologies of fracture surfaces and the cracking path after the V-notched impact test. Martensitic matrix and δ-ferrite lamellas were fractured to form dimples and deep valleys respectively on the fracture surface (see Fig. 2(d)), indicating a ductile fracture [31]. Moreover, Fig. 2(d) shows that the δ-ferrite lamellas on the deep valleys should have capture some propagating cracks and even deflect some of them, leading to rougher fracture surface formed. On the cross section below the surface fracture, delaminated cracks propagated along both prior austenite grain boundaries (PAGBs) and the interfaces of aligned δ-ferrite lamellas and martensite; both cracking paths are perpendicular to the striking direction (see Fig. 2(e)) but parallel to RD. The distance of cracks propagating along the PAGBs and the δ-ferrite into the matrix was approximately 125 μm and 35 μm, respectively. This suggests that the δ-ferrite has a higher resistance to the propagation of cracking during the impact tests. Therefore, the deflection of delaminated cracks, either into elongated δ-ferrite or along the interface of δ-ferrite/martensite, could significantly

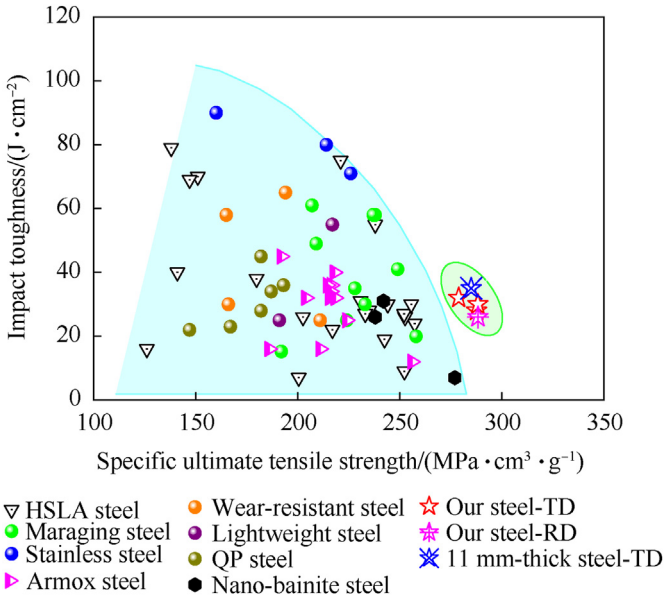

Fig. 1. Specific ultimate tensile strength and impact toughness of studied steel compared with other ultrastrong steels, including high strength low alloyed martensitic steels [17,18], maraging steel [19], stainless steels [20,21], armor steels [22,23], wear-resistant steels [24], lightweight steels [25,26], QP steels [27,28], nano-bainite steels [29]. The '11 mm-thick steel' is the present studied steel having the thickness of 11 mm after a different hot rolling process, from which the standard CVN specimen having the dimension of 10 mm × 10 mm × 55 mm was machined for measuring impact toughness. The densities were calculated by the method proposed in Ref. [30] from their compositions when they were not given in the references.

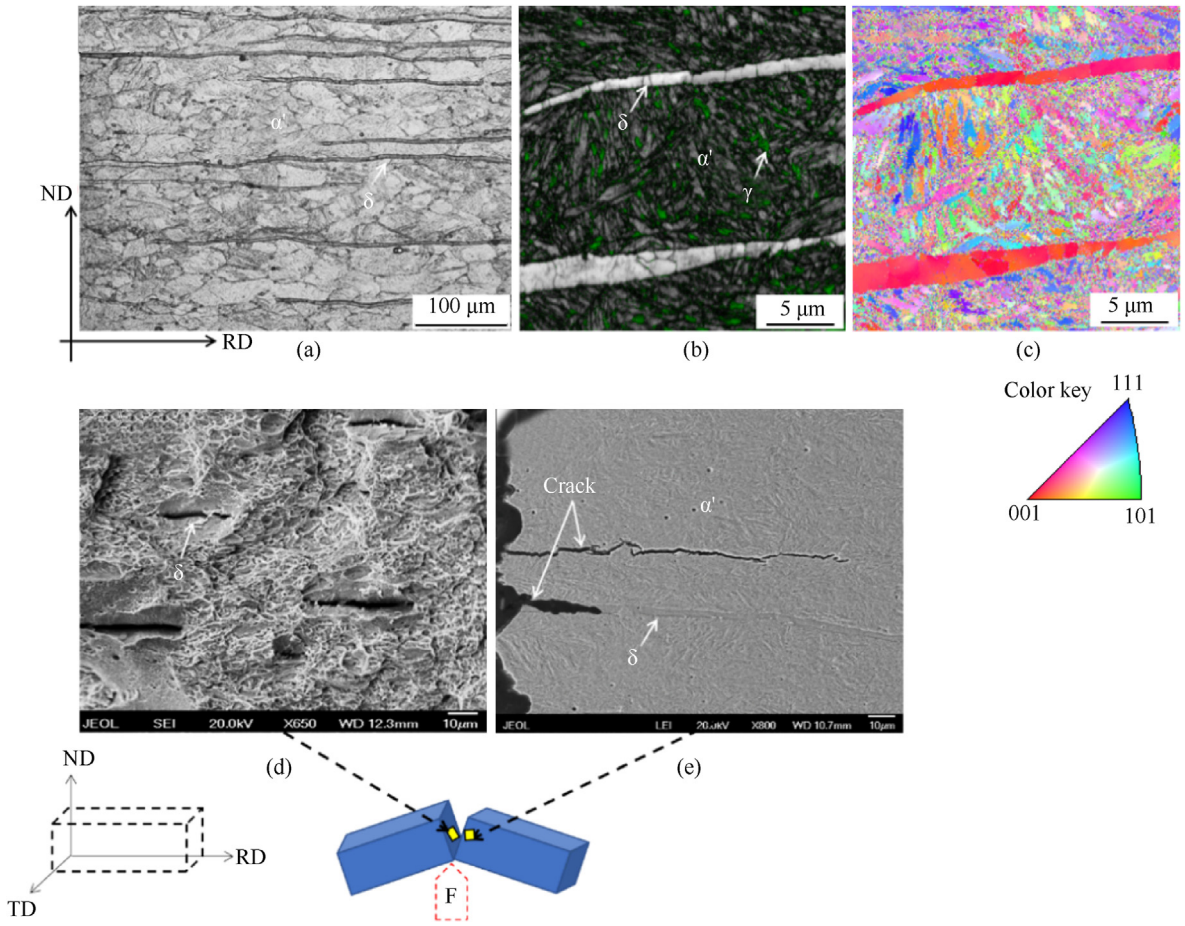

Fig. 2. (a) Optical microscopy; (b), (c) EBSD and (d), (e) SEM results on the microstructures of studied steel before ((a)–(c)) and after ((d)–(e)) the CVN impact test, examined at the positions indicated by the arrows in the sketch map. (a) Tri-phase microstructures comprising martensitic matrix and oriented δ-ferrite lamellas and dispersed RA grains as revealed by the green in (b), EBSD band contrast image overlapped by phase distribution; (c) the corresponding inverse pole figure of (b); (d) the typical fracture surface morphology and the cracking paths below the surface (e). ND, RD and TD represent the normal, rolling and transverse directions.

improve impact toughness when compared with the mere propagation along the PAGBs. This results in higher CVN toughness achieved even at ultrahigh strength and low density than other ultrastrong steels.

3.2. Bulletproof tests

The front and back views of crater on the target steel sheet are shown in Figs. 3(a) and 3(b). Neither penetration nor any visible cracking was observed on the impacted steel, indicating the shooting of bullet was successfully defended. Successful arrest was also indicated by the apparent plastic deformation near the crater. Although adiabatic shear bands often appear in the severely plastically deformed zone during the ballistic tests [32], they were not observed in this case most probably because this steel has high hardness and exceptional work hardening ability [33–35]. The cross-sectional view below the crater in Figs. 3(c) and 3(d) reveal some inner cracks, which propagated over several millimeters mostly perpendicularly to the striking direction and parallel to RD.

RA fractions were examined near the crater at the positions marked by P1, P2, P3, P4 in Fig. 3(c) by using ex-situ high energy XRD. The obtained spectra are shown in Fig. 4(a) and the calculated RA fractions in Fig. 4(b). The latter gradually increase when the examined positions have larger distance to the back surface center of crater as they suffered smaller plastic strain. The microstructures at the positions of P4, P3, P2, P1 near the crater were also examined by EBSD and the results are show in Fig. 5(a) through Fig. 5(d). It is apparent that fewer RA grains survived at the position closer to the back surface center of crater, which is consistent with the HE-XRD results in Figs. 3(a) and 3(b). This is clearly because more plastically strained RA grains are more likely to transform to martensite.

Fig. 6 shows some cracks observed on the RD⊥ND section around the crater after the ballistic test. Figs. 6(b)–6(e) and Figs. 6(f)–6(h) are the SEM and EBSD results respectively showing the propagating path of primary crack starting from 'E' in Fig. 6(a). These cracks propagated both parallelly and perpendicularly to the striking direction of bullet (Fig. 6(b)). The parallelly propagating cracks were blunted by δ-ferrite lamellas, which are perpendicular to the striking direction, by deflecting them into the perpendicular direction, followed by their propagation in δ-ferrite lamellas (Fig. 6(c)) or along the δ/α' interface (Fig. 6(d)) when the cracks encountered them. In addition, some parallel cracks stopped propagation inside martensite matrix, see Fig. 6(e).

It is seen in Figs. 6(f)–6(h) that the perpendicular cracks propagated along prior austenite grain boundaries (PAGBs) and δ/α' interface, which is exactly same to the propagation of delaminated cracks during the CVN impact tests in Fig. 2(e). Furthermore, it was observed that the perpendicular cracks stopped propagation at the

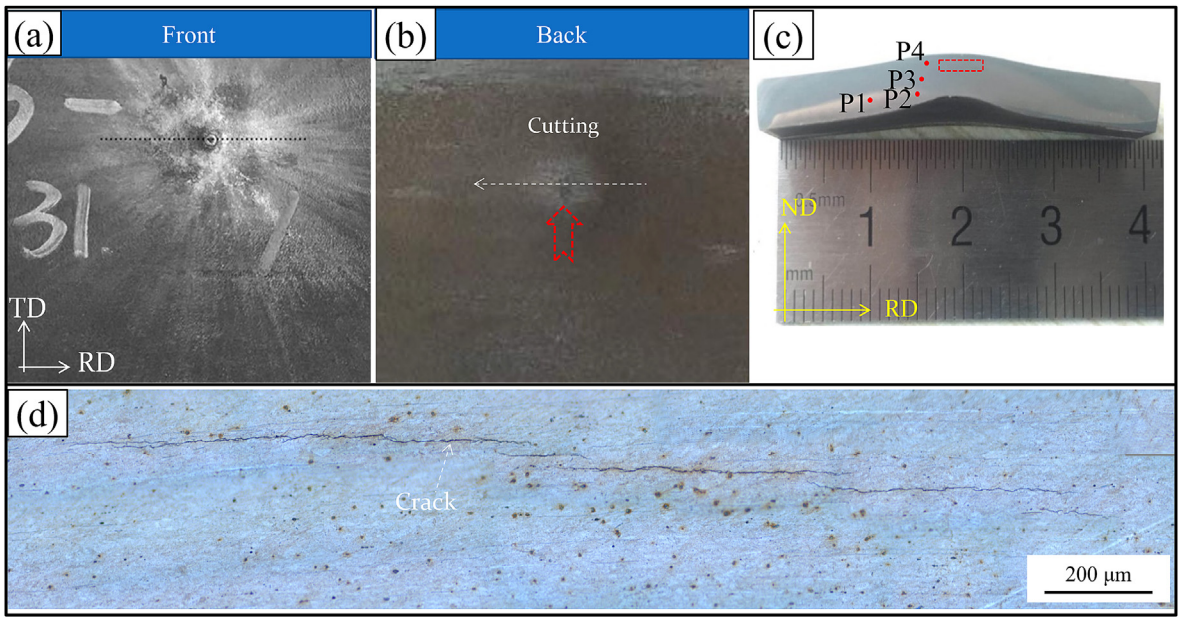

Fig. 3. (a) The front and (b) back views of target steel strip around the crate; (c) The cutting views of target steel strip around the crater along the transverse direction, as indicated in (b); (d) The magnified views for regions marked by red rectangles in (c).

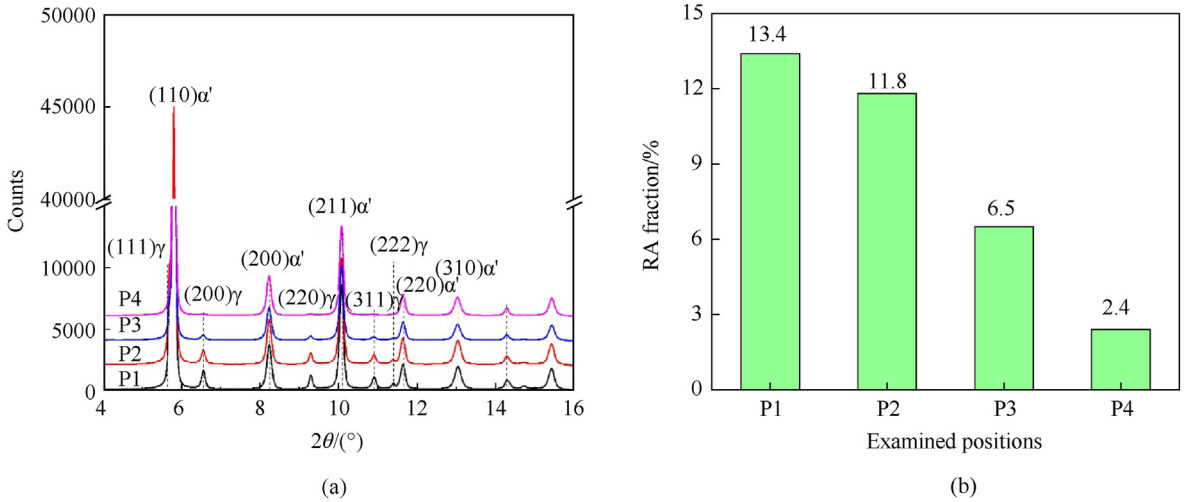

Fig. 4. (a) High energy XRD spectra obtained at the positions of P1, P2, P3, P4 in Fig. 3(c); (b) The calculated RA fractions.

δ/α' interface (see Figs. 6(f) and 6(g)) or inside martensite matrix (see Figs. 6(g) and 6(h)). Fewer RA grains were found near the propagating cracks than those far away from them (see Figs. 6(f) and 6(g)), indicating that more RA grains transformed to martensite at the positions closer to cracks due to more severe plastic strain encountered, which increased the energy required for the propagation of cracks and contributed to improved ballistic performance too.

4. Discussion

The studied lightweight steel indeed exhibits both superior combination of CVN toughness and specific UTS and the desired excellent bulletproof performance that was first achieved at such a reduced density, as expected. The latter is firstly ascribed to ultra-high UTS (2.1 GPa) and hardness (62 HRC) to resist the penetration of bullets and avoid the plugging failure and the prominent strain hardening increment of 1.4 GPa to disperse the impact force of the bullet, the latter is also indicated by the pronounced plastic strain developed near the carter (see Fig. 3(c)). Moreover, the strain rate in the ballistic test is much higher than that in the quasistatic tensile test, leading to even greater strain hardening capability to resist the projectile impact via the release of internal stress, dislocation multiplication and γ-to-α' transformation as concluded in Ref. [9]. Particularly, both the XRD results in Fig. 4 and EBSD results in Fig. 5 confirm that the strain-induced martensite transformation has indeed occurred during the projectile tests since fewer RA grains survived at the positions subjected to greater plastic strain. Particularly, this strain-induced martensite transformation promotes the closure of cracks due to the volume expansion accompanying the transformation, which is documented as transformation-induced crack closure (TICC) [36]. In addition,

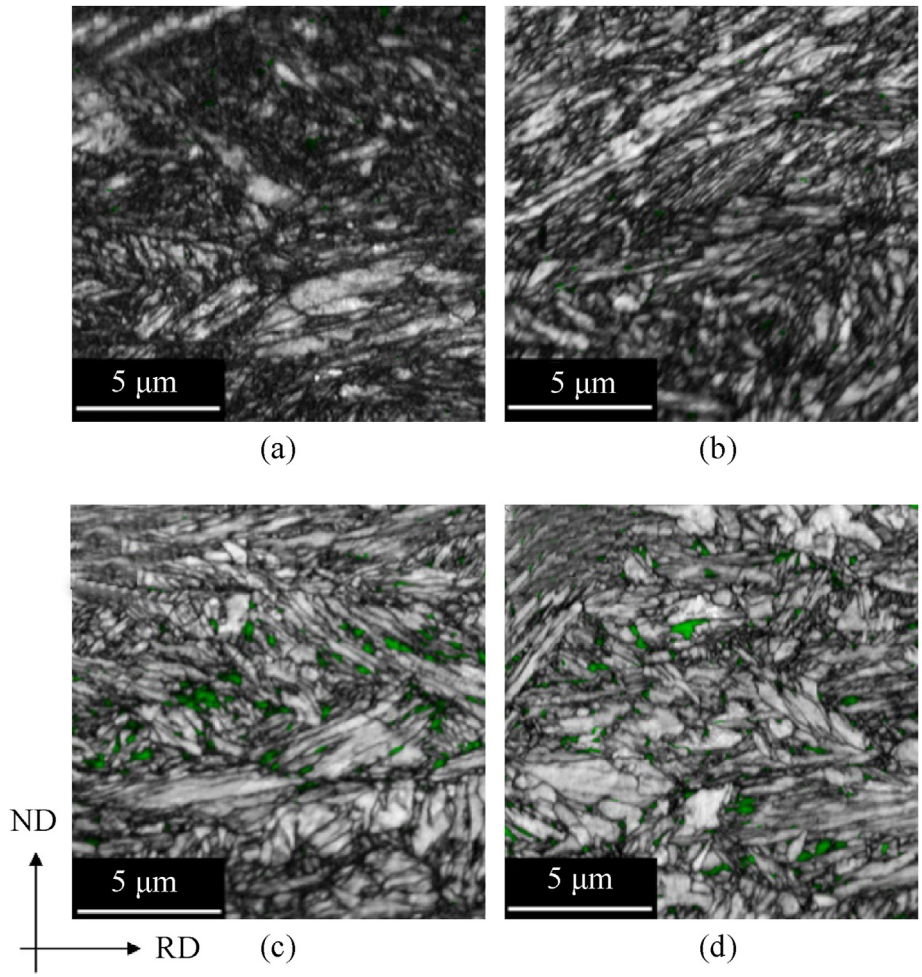

Fig. 5. EBSD band contrast images overlapped with phase distribution for the microstructures examined at the positions of (a) P4, (b) P3, (c) P2, (d) P1 in Fig. 3(c). The green represents retained austenite.

some cracks stopped propagating inside martensite after a zigzag cracking path (Figs. 6(g) and 6(h)), which is attributed to roughness-induced crack closure (RICC) [37].

More importantly, this implies a new toughening mechanism in addition to them, *i.e.* the cracks were deflected and trapped in the δ-lamellas that were extensively distributed in the tri-phase microstructure, leading to the kinetic energy of the bullet absorbed much more effectively since the tip of crack was blunt in the relatively soft δ ferrite, the brittle intergranular cracking was suppressed and the length of cracking path increased significantly, as demonstrated above. When the bullet impact-induced cracks were initiated at either the PAGB or δ/α' interface, they can propagate both parallelly and perpendicularly to the striking direction. The parallel cracks resulted in undesired quick through-thickness fracture. When cracks met the {200} in-plane textured δ-ferrite lamellas, they were then captured and deflected in the direction perpendicular to the striking one and started to propagate inner δ-ferrite (Fig. 6(a) through Fig. 6(c)) or along the δ/α' interface (Figs. 6(d) through 6(g)). These propagating cracks were blunted by the soft δ-layers with more resistance to the cracking than those along the PAGB (see Fig. 2(e)). This is because the {100} cleavage is the natural failure mode of many bcc crystals, including iron [38]. For an example, δ-ferrite in medium-Mn steel was observed to fracture on the {100} planes during the tensile test [39]. In this case, these deflected cracks had to propagate over a much longer distance along the {100} planes of textured δ-ferrite together with more RA grains nearby transformed than those along the striking direction, leading to more energy being consumed before failure. These textured δ ferrite lamellas should also deflect the primary propagating cracks from the striking direction to the one perpendicular to it during the CVN impact test, as confirmed by the deep valleys on the fracture surface (Fig. 2(d)) and the appearance of delaminated cracks along δ/α' interface or within δ-ferrite (Fig. 2(e)).

Since the formation of δ-ferrite results from the low-density design that is realized by adding high contents of Si and Al, one may expect that more textured δ-ferrite lamellas dispersed perpendicularly to the striking direction could capture and deflect the propagating cracks more frequently, which could further improve toughness of lightweight steel with lower density.

5. Conclusions

Contrary to the classical wisdom that the formation of δ-ferrite due to the alloying with high contents of Al and Si often deteriorates mechanical properties of steels [39–43], we conclude that the textured δ-ferrite lamellas in the studied steel can capture the propagating cracks and deflect them so that they propagate along the interface of elongated δ lamella and α' and even into the δ ferrite grains, where they are trapped. This greatly improves both impact fracture toughness and the bulletproof performance of

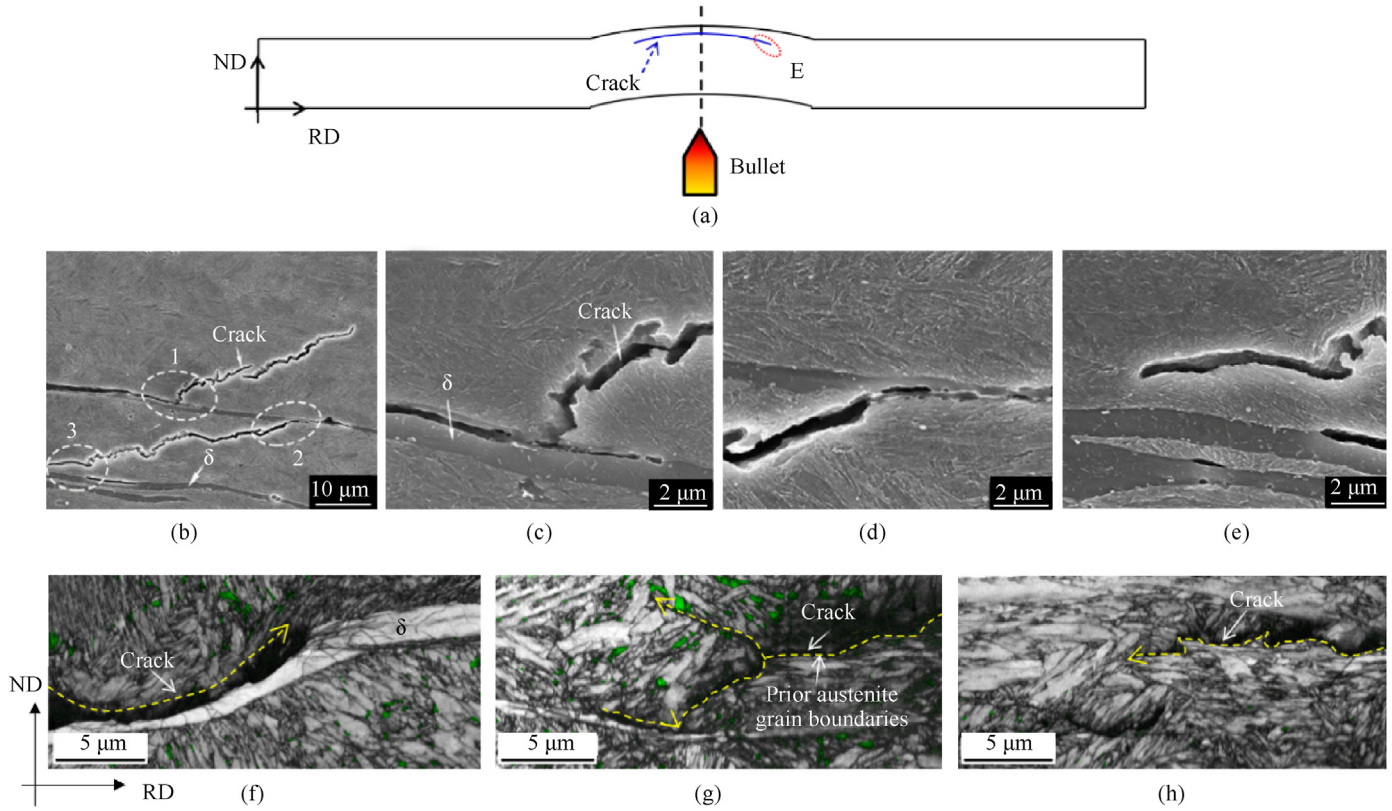

Fig. 6. Microstructures around the crater on the steel sheet after the projectile test: (a) Schematical cutting view around the crater; SEM images ((b), (c), (d), (e)) and EBSD band contrast images overlapped by phase distribution ((f) (g), (h)) on the microstructures at the 'E' of (a) both comprise the propagating cracks. (c), (d) and (e) are the magnified views of '1', '2' and '3' circles in (b) respectively. The green in (f)–(h) represents austenite.

ultrastrong low-density steel. When these δ lamellas are more densely distributed perpendicularly to the striking direction, it may be reasonably expected that the propagating cracks shall be captured, deflected, and trapped more frequently. This leads to greater crack delamination and dynamic energy consumption, suggesting a new microstructural design strategy for improving the toughness and ballistic performance of ultrastrong armor steel with low density.

Author contributions

H.W. Luo supervised the study. B. Hu and H.W. Luo designed the study. B. Hu and G.H. Shen conducted the thermomechanical treatment, the mechanical tests, and the microstructure characterization. B. Hu and H. Luo wrote the paper.

Declaration of competing interest

The authors declare that they have no known competing financial interests or personal relationships that could have appeared to influence the work reported in this paper.

Acknowledgements

Haiwen Luo and Bin Hu acknowledge financial support from National Natural Science Foundation of China (Grant Nos. 51831002, 51904028 and 52233018), China and Fundamental Research Funds for the Central Universities (Grant No. 06500151), China. The present work is related to awarded patents (201910244716.9 in China and US 10793932 in USA).

References

[1] Kim SJ, Hwang EH, Park JS, et al. Inhibiting hydrogen embrittlement in ultra-strong steels for automotive applications by Ni-alloying. NPJ Mater. Degrad. 2019;3:1–7.
[2] Liu L, Yu Q, Wang Z, et al. Making ultrastrong steel tough by grain-boundary delamination. Science 2020;368:1347–52.
[3] Kim HS, Kim H, Kim NJ. Brittle intermetallic compound makes ultrastrong low-density steel with large ductility. Nature 2015;518:77.
[4] Atapek SH. Development of a new armor steel and its ballistic performance. Defense Sci. J. 2013;63(3):271–277.
[5] Naveen Kumar S, Balasubramanian V, Malarvizhi S, Hafeezur Rahman A, Balaguru V. Effect of welding consumables on the ballistic performance of shielded metal arc welded dissimilar armor steel joints. J Mater Eng Perform 2022;31(1):162–79.
[6] Maweja K, Stumpf W. Fracture and ballistic-induced phase transformation in tempered martensitic low-carbon armor steels. Mater Sci Eng, A 2006;432(1–2):158–69.
[7] Zhang Peng, Zhang Zhefeng. Getting tougher in the ultracold. Science 2022;378(6623):947–948.
[8] Bao RQ, Huang X, Huang LJ, Cao CX. Optimisation of hot die forging processes of Ti–10V–2Fe–3Al alloy. Mater Sci Technol 2005;21(4):451–458.
[9] Hu B, Shen GH, Wang Z, Li SL, Wang YD, Luo HW. Ultrahigh tensile strength achieved in a lightweight medium Mn steel via prominent work hardening. J Mater Sci Technol 2023;145:156–164.
[10] Lach E, Koerber G, Scharf M, Bohmann A. Comparison of nitrogen alloyed austenitic steels and high strength armor steels impacted at high velocity. Int J Impact Eng 1999;23:509–17.
[11] Zhang M, Cao W, Dong H, et al. Element partitioning effect on microstructure and mechanical property of the micro-laminated Fe–Mn–Al–C dual phase steel. Mater Sci Eng, A 2016;654:193–202.
[12] Zhang MD, Hu J, Cao WQ, Dong H. Microstructure and mechanical properties of high strength and high toughness micro-laminated dual phase steels. Mater Sci Eng, A 2014;618:168–175.
[13] Xu X, Li J, Zhang W, et al. Structure-Property relationship in a micro-laminated low-density steel for offshore structure. Steel Res Int 2019;90(5):1800515.
[14] Cao WQ, Xu HF, Zhang MD, et al. Low density high strength and high toughness steel with ferrite and martensite laminated structure. In: Advanced high strength steel and press hardening: proceedings of the 3rd international conference on advanced high strength steel and press hardening; 2017. 11–

19. ICHSU2016.
[15] Hu B, Wen HQ, Guo YQ, Wang JY, Sui H, Luo WH. A novel electric pulse pathway to suppress plastic localization and enhance strain hardening of medium Mn steel. Scripta Mater 2022;221:114991.
[16] Cao SJ. Study on equivalent ratio of absorbed energies from Charpy Impact tests for specimens of different sizes. Heat Treatment 2010;25(3):60–4.
[17] Kolla HH, Mishra B, Jena PK, Siva Kumar K, Bhat TB, Srinivas M, Reddy AV. Development of an ultrahigh strength low alloy steel for armour applications. Mater Sci Technol 2011:551–5.
[18] Mandal G, Roy C, Ghosh SK, Chatterjee S. Structure-property relationship in a 2 GPa grade micro-alloyed ultrahigh strength steel. J Alloys Compd 2017;705:817–27.
[19] Handerhan KJ, Moody WMGR. A comparison of the fracture behavior of two heats of the secondary hardening steel AF1410. Metall Mater Trans A 1989;20:105–23.
[20] Xiang S, Wang JP, Sun YL, Yan YY, Huang SG. Effect of ageing process on mechanical properties of martensite precipitation-hardening stainless steel. Adv Mater Res 2010;146:382–5.
[21] Mithieux JD, Godin Hélène, Gourgues-Lorenzon AF, Parrens C. Influence of Nb addition on impact toughness of as-quenched martensitic stainless steel for automotive applications. Mater Sci Forum 2018;941:245–50.
[22] Gupta D, Chattopadhyay S, Amte N, Shingweker A. Development of ARMAPRO ballistic resistant steels – essar steel synergizing with " Make in India " campaign. Ftc March Cvrde Ruby Jubilee Celebration National Technical Seminar on Future Technologies for Combat Vehicles 2017:1–10.
[23] Grujicic M, Arakere A, Ramaswami S, Snipes JS, Yavari R, Yen C-F, Cheeseman BA, Montgomery JS. Gas metal arc welding process modeling and prediction of weld microstructure in MIL A46100 armor-grade martensitic steel. J Mater Eng Perform 2013;22:1541–57.
[24] Haiko O, Javaheri V, Valtonen K, Kaijalainen A, Hannula J, Kömi J. Effect of prior austenite grain size on the abrasive wear resistance of ultra-high strength martensitic steels. Wear 2020;454–455:1–13.
[25] Kalashnikov I, Shalkevich A, Acselrad O, Pereira LC. Chemical composition optimization for austenitic steels of the Fe-Mn-Al-C system. J Mater Eng Perform 2000;9:597–602.
[26] Luo KT, Kao PW, Gan D. Low temperature mechanical properties of Fe-28Mn-5Al-1C alloy. Mater Sci Eng, A 1992;151:15–8.
[27] Dong J, Zhou X, Liu Y, Li C, Liu C, Li H. Effects of quenching-partitioning-tempering treatment on microstructure and mechanical performance of Nb-V-Ti microalloyed ultra-high strength steel. Mater Sci Eng, A 2017;690:283–93.
[28] Gao G, An B, Zhang H, Guo H, Gui X, Bai B. Concurrent enhancement of ductility and toughness in an ultrahigh strength lean alloy steel treated by bainite-based quenching-partitioning-tempering process. Mater Sci Eng, A 2017;702:104–12.
[29] Avishan B, Yazdani S, Caballero FG. Characterization of microstructure and mechanical properties in two different nanostructured bainitic steels. Mater Sci Technol 2015;31:1508–20.
[30] Shen GH, Wen PY, Luo HW. A thermodynamic model on predicting density of medium-Mn steels with experimental verification. J Iron Steel Res Int 2017;24(11):1078–84.
[31] Alkan G, Chae D, Kim SJ. Effect of δ ferrite on impact property of hot-rolled 12Cr–Ni steel. Mater Sci Eng, A 2013;585:39–46.
[32] Yan N, Li Z, Xu Y, Meyers MA. Shear localization in metallic materials at high strain rates. Prog Mater Sci 2020;119:100755.
[33] Jo MC, Kim S, Suh DW, Hong SS, Kim HK, Sohn SS, Lee S. Role of retained austenite on adiabatic shear band formation during high strain rate loading in high-strength bainitic steels. Mater Sci Eng, A 2020;778:139118.
[34] Long BZ, Zhang Y, Guo CH. Enhanced dynamic mechanical properties and resistance to the formation of adiabatic shear band by Cu-rich nano-precipitates in high-strength steels. Int J Plast 2021;138:102924.
[35] Børvik T, Dey S, Clausen AH. Perforation resistance of five different high-strength steel plates subjected to small-arms projectiles. Int J Impact Eng 2009;36:948–64.
[36] Motomichi K, Zhang Z, M Wang M, Ponge D, Raabe D, Tsuzaki K, Noguchi H, Tasan CC. Bone-like crack resistance in hierarchical metastable nanolaminate steels. Science 2017;355:1055–7.
[37] Zhang Z, Koyama M, Wang MM, Tsuzaki K, Tasan CC, Noguchi H. Effects of lamella size and connectivity on fatigue crack resistance of TRIP-Maraging steel. Int J Fatig 2017;100:176–86.
[38] Jr J, Guo Z, Krenn CR, Kim YH. The limits of strength and toughness in steel. ISIJ Int 2001;41:599–611.
[39] Sun B, Palanisamy D, Ponge D, Gaulta B, Fazelic F, Scottc C, Yueb S, Raabea D. Revealing fracture mechanisms of medium manganese steels with and without delta-ferrite. Acta Mater 2019;164:683–96.
[40] Wu ZQ, Ding H, An XH, Han D, Liao XZ. Influence of Al content on the strain-hardening behavior of aged low density Fe–Mn–Al–C steels with high Al content. Mater Sci Eng, A 2015;639:187–91.
[41] Hwang JH, Trang TTT, Lee O, et al. Improvement of strength–ductility balance of B2-strengthened lightweight steel. Acta Mater 2020;191:1–12.
[42] Wang Q, Chen S, Rong L. δ-Ferrite formation and its effect on the mechanical properties of heavy-section AISI 316 stainless steel casting. Metall Mater Trans A 2020;51:2998–3008.
[43] Liu Z, Ma Q, Jiang C, et al. High-temperature creep property deterioration of the alumina-forming austenitic steel: effect of σ phase. Mater Sci Eng, A 2022;846:143126.